ANL/CHM/CP--95786
CONF-980741--

RECEIVED
JUL 30 1998
OSTI

Address for Correspondence:

Prof. George C. Schatz
Department of Chemistry
Northwestern University
Evanston, IL 60208-3113 USA

**Quantum Scattering Studies of Spin-Orbit**

**Effects in the $Cl(^2P) + HCl \rightarrow ClH + Cl(^2P)$ Reaction**

George C. Schatz*

Theoretical Chemistry Group, Chemistry Division,

Argonne National Laboratory, Argonne IL 60439 USA

Patrick McCabe†, J. N. L. Connor

Department of Chemistry, University of Manchester, Manchester M13 9PL, UK

*Visiting Scientist. Permanent address: Department of Chemistry, Northwestern University, Evanston IL 60208-3113 USA

†Present address: Clinical Trial Service Unit, Nuffield Department of Clinical Medicine, University of Oxford, Harkness Building, Radcliffe Infirmary, Woodstock Road, Oxford OX2 6HE, UK

## DISCLAIMER

## Abstract

We present quantum scattering calculations for the Cl + HCl→ ClH + Cl reaction in which we include the three electronic states that correlate asymptotically to the ground state of $Cl(^2P)$ + $HCl(X^1\Sigma^+)$. The potential surfaces and couplings are taken from the recent work of C. S. Maierle, G. C. Schatz, M. S. Gordon, P. McCabe and J. N. L. Connor, J. Chem. Soc. Farad. Trans. (1997) 93, 709. They are based on extensive *ab initio* calculations for geometries in the vicinity of the lowest energy saddle point, and on an electrostatic expansion (plus empirical dispersion and repulsion) for long range geometries including the van der Waals wells. Spin-orbit coupling has been included using a spin-orbit coupling parameter $\lambda$ that is assumed to be independent of nuclear geometry, and Coriolis interactions are incorporated accurately. The scattering calculations use a hyperspherical coordinate coupled channel method in full dimensionality. A J-shifting approximation is employed to convert cumulative reaction probabilities for total angular momentum quantum number J = 1/2 into state selected and thermal rate coefficients. Two issues have been studied: a) the influence of the magnitude of $\lambda$ on the fine-structure resolved cumulative probabilities and rate coefficients (we consider $\lambda$'s that vary from 0 to ±100% of the true Cl value), and b) the transition state resonance spectrum, and its variation with $\lambda$ and with other parameters in the calculations. A surprising result is the existence of a range of $\lambda$ where the cumulative probability for the $^2P_{1/2}$ state of Cl is larger than that for the $^2P_{3/2}$ state, even though $^2P_{1/2}$ is disfavoured by statistical factors and only reacts via nonadiabatic coupling. This result, which is not connected with resonance formation, may arise from coherent mixing of the $\Omega_j = 1/2$ components of the $^2P_{3/2}$ and $^2P_{1/2}$ states in the van der Waals regions. The $^2P_{1/2}$ state dominates for values of $\lambda$ between the statistical and adiabatic limits

when mixing converts $^2P_{1/2}$ into a state that is, for linear geometries, predominantly $^2\Sigma_{1/2}$ near the barrier. We find two significant resonances for total energies below 0.7 eV. They are associated with two quanta of asymmetric stretch excitation of the transition state and with zero or one quanta of bend excitation. These resonances are most prominent (i.e., narrowest) in the adiabatic limit of large $|\lambda|$. For $|\lambda| \approx 0$, the resonances are largely washed out due to strong mixing between attractive fine-structure states which support the resonances and repulsive ones which produce decay.

## I. Introduction

One of the most important recent developments in the quantum theory of gas phase chemical reactions is that it has become possible to carry out converged three dimensional scattering calculations for reactions where two or more potential energy surfaces are coupled together during reaction.[1-6] Such reactions are extremely common in gas phase kinetics when one or both of the reagent species is a radical, and in fact all reactions which have previously been studied using single surface dynamics methods (e.g., $H + H_2$, $F + H_2$, $O + H_2$, $Cl + H_2$, $Cl + HCl$) involve multiple potential surfaces in some sense. Most of these reactions are have several potential surfaces which are asymptotically degenerate (i.e., degenerate in the reagents and/or products). However, these surfaces split when the reagents approach, giving rise to surfaces with different barriers. In this situation, it is usual to ignore surfaces other than the one with the lowest barrier height; however the validity of this approximation is generally not known. A common situation which arises for these reactions is that the surface with the deepest van der Waals wells is not the one with the lowest barrier height. This means there is always a crossing between different potential curves as one moves along the reaction path, which provides an opportunity for significant nonadiabatic coupling. Complicating this picture is the presence of spin-orbit coupling, which partially lifts the asymptotic degeneracy, providing additional mechanisms for nonadiabatic coupling.

There are several levels of sophistication when performing nonadiabatic quantum dynamics calculations on reactions with asymptotically degenerate potential surfaces. The most rigorous approach uses basis functions in which the electronic orbital and spin angular momenta of the separated reagents and products are explicitly included, along with coupling to the orbital and rotational angular momenta of the nuclei. It is this approach which we have adopted (with a few approximations) in our recent work.[3,6] It leads straightforwardly to the inclusion of Coriolis coupling between the basis states, and to the incorporation of electrostatic nonadiabatic and spin-orbit coupling. A simpler approach is to ignore the electronic angular momenta, and thereby regard the electronic degrees of freedom as internal variables without vector properties. This is a commonly used level of treatment;[2,4] it still allows for the inclusion of nonadiabatic and some aspects of spin-orbit coupling, but the electronic part of the Coriolis coupling is not included. Further simplifications involve the use of rotational sudden approximations, or linear models, where the nuclear rotational coupling is missing, and important aspects of the nonadiabatic coupling are lost. This level of treatment was common in quantum scattering calculations done in the late 1970's (reviewed in Ref. 1).

The high level of sophistication in our treatment of electronic/nuclear coupling allows us to study nonadiabatic reactions in ways that have not previously been considered. In the present paper, we present results of quantum scattering calculations which explore two new issues, namely: a) the influence of the magnitude of the spin-orbit coupling parameter $\lambda$ on the fine-structure resolved and cumulative reaction probabilities and rate coefficients, and b) the influence of $\lambda$ and the nonadiabatic coupling on the transition state resonance spectrum. To study these issues, we have performed calculations for the reaction

$$Cl(^2P) + HCl \rightarrow ClH + Cl(^2P)$$

including the three potential surfaces, $1^2A'$, $2^2A'$ and $1^2A''$, which correlate to the ground states of the reagents and products. Cl + HCl is a simple hydrogen transfer reaction which serves as a canonical model both for heavy-light-heavy atom reactions, and for the reactions of halogen atoms with closed shell molecules. We have chosen this reaction in part because we and others have studied its single surface dynamics thoroughly in the past using quantum scattering methods,[7,8] and because it is one of the few reactions for which there are global diabatic potential surfaces and couplings that are valid both near the lowest energy saddle point and in the long range van der Waals regions. Cl + HCl is also of interest because transition state photodetachment measurements[9] have been performed, and the results are suggestive of resonance formation.

Our dynamics calculations are based on a coupled-channel quantum scattering method in hyperspherical coordinates which was introduced in Ref. 3. This follows the scattering formalism of Rebentrost and Lester[10] which explicitly includes all nuclear and electronic angular momenta and their vector couplings. The electronic state expansion uses a diabatic basis, so that geometric phase effects associated with the conical intersection are automatically included.

The diabatic potentials and couplings that we use are from Ref. 6. These were developed using a new approach in which the long range potentials (van der Waals regions) are represented by an electrostatic expansion[11] while the short range potentials (barrier regions) are derived from *ab initio* electronic structure calculations. The electrostatic expansion is developed in a diabatic representation, and the coupling terms in this representation are assumed to be valid even at short range, thereby providing the couplings needed to construct diabatic surfaces at short range using the adiabatic data that come from the *ab initio* calculations. These diabatic surfaces do not include spin-orbit coupling, but it is not difficult to add this, with the assumption that $\lambda$ is independent of nuclear geometry. Justification for this assumption is provided by comparison with recent relativistic *ab initio* calculations, which show a shift in the barrier height due to spin-orbit effects[12] that is similar to our simple treatment.

In the present study we have performed calculations for values of the spin-orbit wavenumber parameter ranging from 0 to ±100% of the true Cl atom value (-588 $cm^{-1}$) so as to determine how the dynamics changes with $\lambda$. We already know[3,6] that the lowest barrier height (that for the surface we denote the $^2\Sigma$ diabat) increases as $\lambda$ becomes more negative, because the spin-orbit Hamiltonian (for negative $\lambda$) preferentially stabilizes the asymptotic $^2P_{3/2}$ state relative to the $^2\Sigma$ barrier, where there is a partial quenching of the spin-orbit effect. A point that will be emphasized in the present paper is the way in which spin-orbit influences the reactivity of $^2P_{1/2}$ relative to $^2P_{3/2}$, as this provides a direct indication of the importance of nonadiabatic dynamics, which have long been of interest in experimental studies of halogen atom reactions.[13] Whilst varying $\lambda$ is an artificial procedure, we will show that it helps us to separate the spin-orbit contribution from other sources of nonadiabaticity, thus clarifying the role of spin-orbit in determining the branching between product fine structure states.. Also, we note that many other atoms have spin orbit wavenumber parameters that are in the range we consider [F(-265 $cm^{-1}$), O(-80 $cm^{-1}$), C(13 $cm^{-1}$), Na(11.5 $cm^{-1}$) and K(38.5 $cm^{-1}$)], so the present calculations can be used to initiate studies of other reactions.

Another point of interest is the ClHCl transition state resonance spectrum. Past work using single surfaces[7,8,14] has demonstrated the existence of one important transition state resonance feature, which corresponds to transition state quantum numbers (0,0,2) where $(v_1,v_2,v_3)$ stands for the (symmetric stretch, bend, antisymmetric stretch) of the ClHCl intermediate. The corresponding (0,0,0) state is not sufficiently stable to exhibit well defined (narrow) features, which means that only states with asymmetric stretch excitation are stabilized sufficiently to support narrow resonances. However what we do not know is whether the presence of multiple coupled potential surfaces will stabilize or destabilize the transition state resonances.

We now summarize the rest of this paper. In Section II, we briefly give details of the global diabatic surfaces and couplings that were developed in Ref. 6. Section III describes the quantum scattering method, and numerical parameters for the coupled channel calculations. The dynamics calculations are presented and discussed in Section IV, whilst Section V contains our conclusions.

**II. Diabatic Potential Surfaces and Couplings**

Figure 1 presents a schematic drawing of the potential curves along the reaction path (for linear geometries) for ClHCl, with the bottom panel showing what occurs for $\lambda = 0$, and the top panel including spin-orbit effects. The reaction gives rise to three doublet adiabatic potentials, namely $1^2A'$, $2^2A'$ and $1^2A''$ (in $C_s$ symmetry), or $^2\Sigma$ and $^2\Pi$ (for linear geometries), all of which correlate to the ground state of $Cl(^2P)$ + HCl in the reagents and products.

Figure 1a shows that the $^2\Sigma$ curve has the lower barrier for hydrogen atom transfer. This corresponds to the singly occupied p-orbital of the reagent Cl atom pointing directly towards the H atom of HCl. In contrast, the singly occupied p-orbital for the $^2\Pi$ curve is perpendicular to the ClHCl axis, so the barrier is much higher (0.7 eV versus 0.4 eV for the scaled surfaces of Ref. 6). This orientation of the p-orbital also gives rise to a more attractive long range potential, due to stronger electrostatic interactions between the doubly occupied p-orbital pointing towards HCl and the positively polarized hydrogen atom in HCl. As a result, the $^2\Sigma$ and $^2\Pi$ curves cross, giving rise to a conical intersection between $1A'$ and $2A'$ (hereafter we drop the spin multiplicity label).

Figure 1b shows how spin-orbit coupling changes the curves. For the Cl atom in the reagents or products, the $^2P_{1/2}$-$^2P_{3/2}$ splitting is 882 $cm^{-1}$, which is about 25% of the $^2\Sigma$ barrier height, and about twice the van der Waals well depth. The asymptotic energy of the $Cl(^2P_{3/2})$ state is lowered by spin-orbit interaction, and since spin-orbit has little effect on the $^2\Sigma$ potential near the barrier top, the overall barrier for the $^2\Sigma$ curve is higher (by approximately 33% of the atomic splitting) than it would be in the absence of spin-orbit. Note that the curves labelled $^2\Sigma_{1/2}$ and $^2\Pi_{3/2}$ correlate with $^2P_{3/2}$ whilst $^2\Pi_{1/2}$ correlates with $^2P_{1/2}$. Because of this, one might expect the reaction probability associated with $Cl(^2P_{1/2})$ to be much smaller than that for $Cl(^2P_{3/2})$. However these adiabatic correlations can, in some situations, be misleading as we will see in Sect. IV.

The global diabatic $\Sigma$ and $\Pi$ potentials and couplings that we use are described in detail in Ref. 6, so here we give just a few key features. The diabats are, as mentioned in the Introduction, based on *ab initio* calculations for geometries near the lowest barrier, and on an electrostatic expansion at long range, with the switch between the two occurring near $r_{HCl} = 4.3\ a_0$, independent of $r_{HCl'}$ (note, however, that the diabats are invariant to interchanging the two Cl's). This region is close to the bottom of the barrier to reaction, with the van der Waals well at larger distances. The lowest energy of the conical intersection occurs somewhat inside the switch region, at $r_{HCl} = 3.4\ a_0$, $r_{HCl'}$=2.6 $a_0$, for linear geometries. The van der Waals minima are located at larger distances, approximately $r_{HCl} = 5.0\ a_0$, $r_{HCl'}$=2.4 $a_0$. The saddle point occurs at $r_{HCl}$=$r_{HCl'}$ = 2.879 $a_0$ on the $\Sigma$ diabat and at $r_{HCl} = r_{HCl'} = 2.953\ a_0$ on the $\Pi$ diabat. Note that the saddle point geometry is bent on the $\Sigma$ diabat (an internal bond angle of 152°), but is linear on the $\Pi$ diabat.

The electronic Hamiltonian is represented in a diabatic basis that is defined using a set of p-orbitals on the reacting Cl atom. The explicit form for the Hamiltonian matrix is:

$$
\begin{array}{cccc}
p_z & p_x & p_y & \\
\left(\begin{array}{ccc}
V_{00} + \frac{2}{5} V_{20} & \frac{1}{5} 6^{1/2} V_{21} & 0 \\
\frac{1}{5} 6^{1/2} V_{21} & V_{00} - \frac{1}{5} V_{20} + \frac{1}{5} 6^{1/2} V_{22} & 0 \\
0 & 0 & V_{00} - \frac{1}{5} V_{20} - \frac{1}{5} 6^{1/2} V_{22}
\end{array}\right) & & &
\begin{array}{c} p_z \\ p_x \\ p_y \end{array}
\end{array}
$$

$$H_{el} = \begin{pmatrix}
V_{00} + \frac{2}{5} V_{20} & \frac{1}{5} 6^{1/2} V_{21} & 0 \\
\frac{1}{5} 6^{1/2} V_{21} & V_{00} - \frac{1}{5} V_{20} + \frac{1}{5} 6^{1/2} V_{22} & 0 \\
0 & 0 & V_{00} - \frac{1}{5} V_{20} - \frac{1}{5} 6^{1/2} V_{22}
\end{pmatrix} \quad (1)$$

where the $V_{\ell m}$ are coefficients of a Legendre expansion of the electrostatic potential in renormalized spherical harmonics, which are functions of the polar angles $\theta_a,\phi_a$ that locate the orientation of the singly occupied p orbital. $V_{00}$ and $V_{20}$ are obtained from the $\Sigma$ and $\Pi$ diabats using the formulae: $V_{00} = (V_\Sigma+2V_\Pi)/3$ and $V_{20} = 5/3(V_\Sigma - V_\Pi)$. The interaction terms $V_{21}$ and $V_{22}$ are taken from the electrostatic potentials given in Ref. 11. They vanish for linear geometries, and drop off as $R^{-4}$, where R is the Jacobi distance the HCl centre of mass to Cl.

## III. Quantum Reactive Scattering Calculations

### A. *Method*

The quantum scattering method we use is the same as that in Ref. 6, which is very similar to the technique described by one of us[3] in an earlier study of Cl + HCl using multiple potential surfaces. Here we describe the method briefly so that notation can be introduced to indicate the calculations we have done, and for our discussion of the results.

We use the notation of Rebentrost and Lester[10] wherein the electronic orbital angular momentum vector of the atom A is denoted **L**, the electron spin angular momentum is denoted **S**, the nuclear rotational angular momentum of the diatomic BC is denoted **N**, and the nuclear orbital angular momentum of A relative to BC is denoted $\boldsymbol{\ell}$. The electronic total angular momentum is denoted **j**, and the electronic plus nuclear total angular momentum is denoted **J**, so that $\mathbf{j} = \mathbf{L} + \mathbf{S}$, and $\mathbf{J} = \mathbf{j} + \mathbf{N} + \boldsymbol{\ell}$. The corresponding angular momentum quantum numbers are denoted L, S, N, $\ell$, j, J. In the present application L = 1 and S = 1/2 in the pure precession limit so that j = 1/2 or 3/2. The allowed values for the remaining quantum numbers are N = 0,1,2, . . . , $\ell$ = 0,1,2, . . . and J = 1/2, 3/2, 5/2 . . . (or sometimes J= 3/2, 5/2, 7/2,...). Body-fixed projection quantum numbers associated with N, j and J are $\Omega_N$, $\Omega_j$, and $\Omega$, respectively. Note that $\Omega=\Omega_N + \Omega_j$, and the body-fixed z axis is chosen to be along the Jacobi vector **R** from the center of mass of the diatom to the atom.

In terms of these quantum numbers, the body-fixed electronic states $|j\Omega_j\rangle$ are related to the spin and orbital parts of the electronic wavefunctions by

$$|j\Omega_j\rangle = \sum_{\Lambda,\Sigma} |L\Lambda\rangle |S\Sigma\rangle\langle L\Lambda S\Sigma | j\Omega_j\rangle \tag{2}$$

where $<l_1m_1l_2m_2 | l_3m_3>$ is a Clebsch-Gordan coefficient. The labels L=1, S=1/2 have been omitted from $|j\Omega_j\rangle$ and the following equations since they have fixed values. We use the states (2) to represent the electronic Hamiltonian, and as a starting point for the coupled channel expansion.

If we now assume that **R** is mass-scaled,[15] and define **r** be the mass-scaled diatom internuclear vector, then the Hamiltonian is given by

$$H = P^2/2\mu + \ell^2/2\mu R^2 + p^2/2\mu + N^2/2\mu r^2 + H_{el} + H_{so} \tag{3}$$

where $\mu$ is the scaled reduced mass,[15] P and p are the radial momenta associated with the distances R and r, respectively, $H_{el}$ is the nonrelativistic electronic Hamiltonian, and $H_{so}$ is the spin-orbit Hamiltonian. The Hamiltonian (3) neglects mass-polarization terms in the electronic Hamiltonian,[10] which are not likely to be important for the low energy processes we are considering.

We next replace $\ell$ by $\mathbf{J} - \mathbf{j} - \mathbf{N}$ in the centrifugal term in (3), which gives

$$\ell^2/2\mu R^2 = (\mathbf{J}^2 + \mathbf{j}^2 + \mathbf{N}^2)/2\mu R^2 - (2\mathbf{J}\cdot\mathbf{j} + 2\mathbf{J}\cdot\mathbf{N} - 2\mathbf{N}\cdot\mathbf{j})/2\mu R^2 \qquad (4)$$

The cross terms in (4) produce three types of Coriolis coupling: orbital-electronic, orbital-rotational, and electronic-rotational. We evaluate all these terms accurately in the coupled-channel expansion given below.

The electronic Hamiltonian $H_{el}$ in (3) is defined using Eq. (1). When expressed in terms of the basis functions $|j,\Omega_j\rangle$ of Eq. (2), we obtain the results in Table 1 (which include a spin-orbit energy adjustment discussed below). Note that in this representation, $V_{21}$ and $V_{22}$ only appear in off-diagonal terms, but $V_{20}$ appears both in the diagonal and off-diagonal terms.

The spin-orbit Hamiltonian $H_{so}$ is taken in the usual form

$$H_{so} = \lambda\, \mathbf{L}\cdot\mathbf{S} = \frac{1}{2}\lambda\, (\mathbf{j}^2\text{-}\mathbf{L}^2\text{-}\mathbf{S}^2) \qquad (5)$$

where the spin-orbit parameter $\lambda$ is assumed to be constant, independent of the internuclear distances. The atomic splitting of the $^2P_{1/2}$ - $^2P_{3/2}$ states is 0.109 eV, which means that $\lambda$ is -0.073 eV. In the

$|j\,\Omega_j\rangle$ basis set, the matrix elements of Eq. (5) are easily evaluated, giving $E_{so}= \frac{1}{2}\lambda[j(j+1)-L(L+1)-S(S+1)]$ along the diagonal of the matrix, and zero for all off-diagonal matrix elements. It is convenient to add $-\frac{1}{2}\lambda$ to $E_{so}$, so that the $^2P_{3/2}$ state has zero energy. This makes the contributions of $H_{so}$ to Table 1 nonzero only for the diagonal terms with $j = 1/2$, $\Omega_j = \pm 1/2$.

*B. Coupled Channel Expansion*

We begin by coupling the electronic states in Eq. (2) with angular eigenstates associated with the rotational and orbital motion of the nuclei. To do this we couple the vectors **j** and **N**, to form a resultant vector **F** where **F** = **j** + **N**. Note that the z-projection quantum number of **F** along **R** is $\Omega$. The resulting electron-nuclear wavefunction associated with F and $\Omega$ is given by

$$|\,NjF\Omega\rangle = \sum_{\Omega_N\Omega_j} |\,N\Omega_N\rangle\,|\,j\Omega_j\rangle\langle N\Omega_N j\Omega_j\,|\,F\Omega\rangle \tag{6}$$

where $|N\Omega_N>$ is a rotational state ket.

We can now write down the coupled channel expansion for the wavefunction associated with each partial wave J and space fixed z projection quantum number M:

$$\Psi^{JM}_{vNjF\Omega} = \sum_{v'N'j'F'\Omega'} D^{J}_{M\Omega'}(\varphi,\theta,0)\,\Phi_{v'N'}(r)\,|\,N'j'F'\Omega'\rangle\, g^{JvNjF\Omega}_{v'N'j'F'\Omega'}(R) \tag{7}$$

where D is a rotation matrix that depends on the polar angles $\theta$, $\phi$ associated with **R**, $\Phi$ is an eigenfunction of the BC rovibrational Hamiltonian, and g is an R-dependent expansion coefficient which is determined numerically by solving a set of coupled Schrödinger equations. In the present case, the Schrödinger equation for the isolated BC molecule is:

$$\left[\frac{P^2}{2\mu} + \frac{N(N+1)\hbar^2}{2\mu r^2} + v(r)\right]\Phi_{vN}(r) = \varepsilon_{vN}\,\Phi_{vN}(r) \tag{8}$$

where $v(r)$ is the diatomic internuclear potential and v = 0,1,2,. . .

We next substitute Eq. (7) into the Schrödinger equation, and use the Hamiltonian in Eq. (3), to obtain the coupled channel equations

$$\frac{d^2\mathbf{g}}{dR^2} = \mathbf{U}\mathbf{g} \tag{9}$$

where **g** is the matrix of expansion coefficients, and **U** is a matrix that may be written in the form:

$$(\mathbf{U})_{tt'} = -\frac{2\mu}{\hbar^2}(E - \varepsilon_{vN})\delta_{tt'} + (\mathbf{U}^{e\ell})_{tt'} + (\mathbf{U}^{so})_{tt'} + (\mathbf{U}^{co})_{tt'} \tag{10}$$

Here we use the collective index "t" to denote the set of quantum numbers (vNjFΩ). In Eq. (10), the first term contains the total energy E, the second term includes the electrostatic potential couplings induced by the difference between $H_{el}$ and v(r), the third describes spin-orbit effects and the fourth describes Coriolis effects. Specific expressions for the second, third and fourth terms are:

(a) for the *electrostatic terms:*

$$(\mathbf{U}^{e\ell})_{tt'} = \frac{2\mu}{\hbar^2}\langle D^J_{M\Omega} \,|\, \langle \Phi_{vN} \,|\, \langle NjF\Omega \,|\, H_{e\ell} - v(r) \,|\, N'j'F'\Omega' \rangle \,|\, \Phi_{v'N'} \rangle \,|\, D^J_{M\Omega'} \rangle \tag{11}$$

(b) for the *spin-orbit terms*:

$$(\mathbf{U}^{so})_{tt'} = \frac{\mu\lambda}{\hbar^2}[j(j+1) - L(L+1) - S(S+1)]\,\delta_{tt'} \tag{12}$$

(c) for the *Coriolis terms*

$$\begin{aligned}(\mathbf{U}^{co})_{tt'} &= \frac{J(J+1) + F(F+1) - 2\Omega^2}{R^2}\,\delta_{tt'} \\ &\quad - \frac{2}{R^2}[\,\xi_-(J,\Omega')\xi_-(F,\Omega')\,\delta_{\Omega,\Omega'-1} + \xi_+(J,\Omega')\xi_+(F,\Omega')\,\delta_{\Omega,\Omega'+1}]\,\delta_{FF'}\delta_{NN'}\delta_{jj'}\delta_{vv'}\end{aligned} \tag{13}$$

where $\xi_{\pm}(J,\Omega) = [J(J+1) - \Omega(\Omega \pm 1)]^{1/2}$. Note that in deriving Eq. (13) the Coriolis Hamiltonian in Eq. (3) has been simplified by use of **F** and the angular momentum eigenfunctions in Eq. (6).

Parity decoupling may be introduced into the coupled channel equations by generalizing the theory for single surface scattering.[15] In particular, parity adapted rotation matrices are used in Eq. (7). This leads to a factorization of the problem into two smaller problems, each with an equal number of channels (for half-odd integer J values). In the present calculations we have approximated the parity decoupling by using basis functions of the form $1/\sqrt{2}\,(|j\Omega_j\rangle \pm |j{-}\Omega_j\rangle)$. When the matrix in Table 1 is reexpressed in terms of these functions, it is necessary to neglect terms involving $V_{22}$ (a relatively small term) in order to decouple into two equivalent parity subblocks. One of the resulting subblocks is identical to the elements in Table 1 that refer only to positive $\Omega_j$'s, and the other to negative $\Omega_j$'s. Each subblock gives the same cumulative probabilities, so only one has been explicitly considered in our calculations.

### C. *Electrostatic Coupling Matrix*

To relate the matrix elements in Eq. (11) to those in Table 1, we substitute Eq. (6) into (11), thereby converting the matrix elements to the basis $|j\Omega_j\rangle$. Assuming that the primed and unprimed variables in the new Eq. (11) refer to the same arrangement channel $\alpha$, then the Wigner rotation matrices are orthogonal, and Eq. (11) reduces to:

$$(U^{e\ell})_{tt'} = \frac{2\mu}{\hbar^2} \sum_{\Omega_N\Omega_j} \sum_{\Omega_{N'}\Omega_{j'}} \langle N\Omega_N j\Omega_j \mid F\Omega\rangle \langle N'\Omega_{N'} j'\Omega_{j'} \mid F'\Omega'\rangle \times \langle \Phi_{vN} \mid \langle N\Omega_N \mid \langle j\Omega_j \mid H_{e\ell} - v(r) \mid j'\Omega_{j'}\rangle \mid N'\Omega_{N'}\rangle \mid \Phi_{v'N'}\rangle \tag{14}$$

If the primed and unprimed variables refer to different arrangement channels, then the overlap of rotation matrices yields d-matrices that should be inserted into the middle of Eq. (14) as described in Ref. 3.

*D. Reactive Scattering and Reaction Probabilities*

The coupled channel equations given by Eq. (9) are appropriate for the description of *nonreactive* atom-diatom scattering. They must be modified for *reactive* collisions because the use of isolated BC rovibrational eigenstates for expanding the wavefunction is inappropriate for product AB + C states. To treat reactive problems we introduce Delves' hyperspherical coordinates,[16] following the theory given previously for single surface reactions by one of us[17] and with Koizumi.[18] The generalization to multisurface problems is identical to that described in Ref. 3 so we omit details. The final outcome of the calculations is the scattering matrix **S** which is labelled by initial and final values of the quantum numbers v,N,j,F,Ω and by the arrangement channel index $\alpha$. The partial wave cumulative reaction probability $P^J_{cum}$ which is needed to calculate rate coefficients, is given by

$$P^J_{cum}(E) = \sum_{tt'} P^J_{\alpha t \alpha' t'}(E) \tag{15}$$

where the sums are over all open states at the energy E and the arrangement channel indices $\alpha$ and $\alpha'$ are chosen to be appropriate for reaction. The partial wave state-to-state reaction probabilities are related to the S matrix elements by

$$P^J_{\alpha t \alpha' t'}(E) = |S^J_{\alpha t \alpha' t'}(E)|^2 \tag{16}$$

We also define cumulative probabilities $P^J_{cum}(E;j,j')$that are labeled by the initial and final values of the electronic quantum number (j and j′) by restricting the sum in (15) appropriately.

*E. Thermal Rate Coefficients*

The multisurface thermal rate coefficient k(T) at temperature T is related to the cumulative probability by the standard formula

$$k(T) = \frac{1}{hQ^{nu}_{reag}(T)Q^{e\ell}_{reag}(T)} \int_0^\infty P_{cum}(E)\exp(-E/k_BT)\,dE \tag{17}$$

where $Q^{nu}_{reag}(T)$ is the reagent nuclear partition function per unit volume (describing translational, vibrational and rotational motions), and $Q^{el}_{reag}(T)$ is the corresponding reagent electronic partition function. We measure energies relative to the $^2P_{3/2}$ state of Cl, and recall that $j = 3/2$ has a degeneracy of 4 while $j= 1/2$ has a degeneracy of 2, then $Q^{el}_{reag}(T) = 4 + 2\exp(3\lambda/2k_BT)$. We also define state selected rate coefficients $k(T;j,j')$ that are labelled by the initial and final values of the electronic quantum numbers (j and j′) using the cumulative probabilities $P^J_{cum}(E;j,j')$ from the previous section, and replacing $Q^{e\ell}_{reag}(T)$ by the electronic partition function $Q^{el}_{reag}(T;j)$ appropriate for the initial quantum number j in Eq. (17), i.e., $Q^{el}_{reag}(T;j=3/2) = 4$ and $Q^{el}_{reag}(T;j= 1/2) = 2\exp(3\lambda/2k_BT)$.

The cumulative probability $P_{cum}(E)$ in Eq. (17) is a weighted sum over partial waves of $P^J_{cum}(E)$:

$$P_{cum}(E) = \sum_J (2J+1)\, P^J_{cum}(E) \tag{18}$$

In the present application, we have used the $J=\frac{1}{2}$ reaction probability to determine the reaction probabilities for $J > \frac{1}{2}$ by means of the J-shifting approximation,[19]

$$P^J_{cum}(E) \approx P^{J=1/2}_{cum}(E - E^J_{rot} + E^{J=1/2}_{rot}) \qquad J = \frac{1}{2}, \frac{3}{2}, \frac{5}{2}, \ldots \tag{19}$$

where $E^J_{rot}$ is the rotational-electronic energy of the $ClHCl^{\ddagger}$ complex for angular momentum quantum number J. We approximated $E^J_{rot}$ by $B_e^{\ddagger}J(J+1)$ where $B_e^{\ddagger} = 1.4 \times 10^{-5}$ eV is the rotor constant associated with the saddle point on the $\Sigma$ diabat (this value is actually that for the BCMR potential of Ref. 20). Other details of the rate coefficient calculations including the inclusion of bend excited states (having $|\Omega_N|>0$), and the accuracy of J-shifting (typically 20%), have been discussed previously.[6,19]

*F. Basis sets and Numerical Parameters*

Most of our scattering computations were done using a basis of 244 states, consisting of rotational states N=0-13 for vibrational state v=0, and N=0-7 for v=1 for each of the two Cl + HCl arrangement channels. We also present results for a 172 state basis set ($N_{max}$=9 for v=0, $N_{max}$=5 for v=1) and for a 292 state basis set ($N_{max}$=13 for v=0 and $N_{max}$=11 for v=1). These three basis sets will be used to estimate the degree of convergence of the results. In addition, we have examined the effect of using two different reference potentials to generate the underlying hyperspherical basis functions. All of the results that we present below use the average electronic potential $V_{00}$ from Eq. (1) as the reference potential, but we also did calculations using $V_\Sigma$ (which was employed in our previous work[6] with smaller basis sets). The scattering results are generally in good agreement ($P^J_{cum}$ is within 20% for nonresonant scattering for E < 0.60 eV); however one difference is that the $V_\Sigma$-based results show additional resonances close to the reaction threshold (i.e., for E well below the energy range where the resonances to be discussed later occur). These additional resonances only appear when a large number of rotational states are included in the v=1 basis ($N_{max} \geq 7$), and only when $V_{21}$ is included in the Hamiltonian. For smaller $N_{max}$ values, the $V_{\Sigma}$-based results do not exhibit additional resonances and are then similar to the $V_{00}$ results. An analysis of the dependence of the hyperspherical adiabatic states on hyperradius suggests that the additional resonances are due to spurious eigenvalues of the Hamiltonian matrix which arise from overcompleteness of the basis set. We therefore conclude that these additional resonances obtained from the $V_{\Sigma}$-based calculations are not physically significant. As a result, we only use below the $V_{00}$-based results for studying the resonances at higher E.

The complete set of $^2P$ electronic states appropriate for J=1/2 was used in all calculations, although it was only necessary to consider one of the two identical parity components. The cumulative probabilities are multiplied by two when calculating rate coefficients in order to include the other parity component. The masses used in the computations are $m_H$=1.008 u and $m_{Cl}$ = 34.969 u.

## IV. Results and Discussion

### A. Cumulative Reaction Probabilities

Figure 2 presents the cumulative reaction probability $P^J_{cum}(E)$ for J = 1/2 as a function of E from our multisurface calculations, comparing results from the 292 and 244 basis sets. Also plotted are the fine structure state selected cumulative probabilities $P^J_{cum}(E;j,j')$ for J = 1/2, with the quantum numbers j and j′ chosen to be j = j′ = 3/2, j = j′ = 1/2, and j = 3/2, j′ = 1/2. Note that microscopic reversibility requires the j = 1/2, j′ = 3/2 cumulative probability to equal that for j = 3/2, j′ =1/2.

The $P^J_{cum}(E)$ and $j = j' = 3/2$ cumulative probabilities show that the effective reaction threshold is near E = 0.37 eV. At higher E, there is a gradual rise in the probabilities, along with broader peaks near E = 0.58 eV and 0.61 eV. These peaks may be assigned to resonances associated with the transition state region of the $\Sigma$ diabat, as discussed in Section IV.C. The cumulative probabilities for 244 and 292 states agree within a few percent for E < 0.55 eV, and are still in good agreement for E < 0.65 eV. This indicates good convergence with respect to basis set size.

The fine-structure-resolved cumulative probabilities for $j = j' = 1/2$ and $j = 3/2, j' = 1/2$ are always much smaller than the $j = j' = 3/2$ one, and the resonance structure is less noticeable. The small values of the $j = j' = 1/2$ and $j = 3/2, j' = 1/2$ cumulative probabilities relative to $j = j' = 3/2$ is the expected behaviour if the electronic states evolve adiabatically between the reagents and products, since the reactive flux connecting $j = j' = 3/2$ can cross the lowest barrier by a purely adiabatic route.

**B. Variation of Cumulative Reaction Probabilities with Spin-Orbit Parameter**

Figure 3 presents results analogous to those in Fig. 2 for four different values of the spin-orbit parameter $\lambda$. From here on, we express $\lambda$ in terms of a linear scaling parameter s, where $\lambda = s\,\lambda_{Cl}$ and $\lambda_{Cl}$ is the correct spin-orbit parameter for (-0.073 eV). The values chosen for s are -0.5, 0.0, 0.1 and 1.0, where for negative s the ${}^2P_{1/2}$ state is lower in energy than ${}^2P_{3/2}$ (however we still define ${}^2P_{3/2}$ to have zero energy). The results in Fig. 3 show two important trends. Firstly, as s increases, the cumulative probabilities, including both direct and resonance features, shift linearly to higher E, with the energy shift being $\approx -\frac{1}{2}\lambda$. This is the previously studied[3,6] energy shift of the barrier height of the $\Sigma$ diabat relative to the ${}^2P_{3/2}$ state, as described in Sect. II. Secondly, for E $\approx$

0.40 eV, the 1/2→1/2 cumulative probability is larger than 3/2→1/2, and 3/2→3/2 for s = -0.5, then it is smaller for s = 0.0, it is larger than the others for s = 0.1, and finally it drops to nearly zero for s = 1.0. The 3/2→3/2 cumulative probability does approximately the reverse of 1/2→1/2, being larger for s=1.0 and s=0.0, and smaller for s=-0.5 and 0.1.

The unusual behaviour in Fig. 3 is further illustrated in Figure 4, where we plot each cumulative probability as a function of s (with $-1 \leq s \leq 1$) for E = 0.40 eV. The results in Fig. 4 were obtained from 172 state calculations, but are not significantly different from the 244 state results. Fig. 4 shows that the 1/2→1/2 cumulative probability is largest for negative s values, with a dip at s=-0.05, then it has a peak between s=0.05 and s=0.1, before dropping to near zero at s=1.0. The 3/2→3/2 cumulative probability starts out small for s=-1.0, then exhibits a sharp peak at s=-0.05, with a modest dip on either side of the peak, and then approaches $P^J_{cum}(E)$ near s=1.0. In contrast to the peaks and dips in the state-resolved probabilities, $P^J_{cum}(E)$ decreases smoothly and monotonically with s; this is expected because of the decrease in barrier height of the $\Sigma$ diabat relative to $^2P_{3/2}$ with increasing $\lambda$.

The behaviour in Figs. 3 and 4 can be understood from the way in which the fine structure states evolve from the asymptotic region to the barrier top of the $\Sigma$ diabat. To simplify the analysis, let us consider the Hamiltonian matrix in Table 1 for linear geometries where $V_{21}$ and $V_{22}$ are identically zero. In this case, the only source of coupling between states with different $(j, \Omega_j)$ is $V_{20}$. Now $V_{20}$ is proportional to the "difference potential" $V_\Sigma - V_\Pi$, and thus vanishes asymptotically. This means that the $|j,\Omega_j\rangle$ states are true eigenstates asymptotically; in particular there are three states that we need to consider (for one parity subblock), namely j=3/2, $\Omega_j$=3/2 and j=3/2, $\Omega_j$=1/2, and j=1/2, $\Omega_j$=1/2. (Note that the parity basis functions involve symmetric or antisymmetric linear combination of functions with positive and negative values of $\Omega_j$ as explained previously, so the sign of $\Omega_j$ isn't meaningful in this list.) Of these three states, we note from the structure of Table 1 that only two states are coupled by $V_{20}$, namely the two with $\Omega_j$=1/2. This means that the $\Omega_j$=3/2 state is uncoupled to the other states except for Coriolis coupling, which is weak for J = 1/2 . The $\Omega_j$=3/2 state correlates with $\Pi_{3/2}$, and it thus has the attractive van der Waals wells at large distances and the high reaction barrier at short range shown in Fig. 1. This state should therefore have low reactivity.

The asymptotic states having $\Omega_j$=1/2 correlate with $\Sigma_{1/2}$ and $\Pi_{1/2}$ at short range. Whether this evolution from $^2P_{3/2}$ and $^2P_{1/2}$ to $\Sigma_{1/2}$ and $\Pi_{1/2}$, respectively, is adiabatic or not depends in large measure on the smallness of the dimensionless parameter $\zeta$, defined by

$$\zeta = \frac{\text{coupling term in Table 1}}{\text{spin-orbit energy separation}} = \frac{\frac{\sqrt{2}}{5}|V_{20}|}{\frac{3}{2}|\lambda|} \tag{20}$$

In Fig. 5(a), we show $\zeta$ as a function of the (unscaled) Jacobi coordinate R (for linear geometry, with $r_{HCl}$ at its equilibrium value of 2.40 $a_0$), whilst Fig. 5(b) displays the three adiabatic potential functions for s=1.0 which have $\Omega_j$ = 1/2, and 3/2. Fig. 5(b) is similar to Fig. 1, at least for geometries outside the conical intersection, i.e., R > 5.9 $a_0$. It is evident from Fig. 5(a) that $\zeta$<1 for all R beyond the conical intersection. This suggests that adiabatic behaviour should prevail, as indeed is observed. If s is decreased to 0.1, then the values along the ordinate of Fig. 5 are multiplied by 10, and $\zeta$>1 for R values in the van der Waals region, suggesting significant nonadiabatic interaction occurs there. Still smaller values of s lead to even larger values of $\zeta$, and in the limit s=0, the states are completely mixed, i.e., we obtain statistical behaviour in this limit, with the 2:1 ratio of j=3/2 :1/2 degeneracies giving ratios of 4:2:1 for the 3/2→3/2: 3/2→1/2: 1/2→1/2 cumulative probabilities.

To test these suggestions concerning the correlation between the asymptotic states and the states closer in, we have used our hyperspherical scattering program to examine the scattering wavefunction for a variety of asymptotic states for both linear and nonlinear geometries. When the asymptotic state is $^2P_{1/2}$, we find the scattering wavefunction shows substantial mixing between j=3/2 and j=1/2 (the precise details depend on the value of $\lambda$) when the inner repulsive wall of the van der Waals well has been reached. This is consistent with the behaviour in Fig. 5.

Our analysis of the importance of nonadiabatic coupling between $\Sigma_{1/2}$ and $\Pi_{1/2}$ does not depend on the sign of s. However it is important to note that for s<0, the lower energy $\Omega_j$=1/2 state has $\Pi_{1/2}$ character in the van der Waals region and $\Sigma_{1/2}$ closer in, whereas for s>0, the lower energy $\Omega_j$=1/2 state is $\Sigma_{1/2}$ both at long and short range. This means that the possibility of nonadiabatic dynamics is more important for s<0 than for s>0. Fig. 4 confirms this in the sense that the 1/2→1/2 cumulative probability contributes less (in per cent) to $P^J_{cum}(E)$ for s=-1.0 than does 3/2→3/2 at s=1.0.

Perhaps the most surprising results in Figs. 3 and 4 are for s just slightly above or slightly below zero, as here we see behaviour that is neither adiabatic nor statistical, and which does not interpolate monotonically between the two limits. This behaviour is different from what was observed in Ref. 3 where surfaces without a conical intersection and van der Waals wells gave cumulative probabilities that evolved monotonically from the statistical to the adiabatic limit, with 3/2→3/2 always being the dominant probability (for s>0). This suggests that the results in Figs. 3 and 4 for s≈0 may arise from quantum coherence in the interaction between the two $\Omega_j$=1/2 states.

What we mean by this is that there is a range of s values where $\zeta$ is large enough to cause substantial (>50%) population transfer between the two states during the approach phase of the collision, thereby favouring the nonadiabatic process. Larger values of $|s|$ give adiabatic behaviour, whilst smaller values leads to continuous cycling of flux between the two states, leading to statistical behavior. This type of behaviour was not observed in Ref. 3 because there were no van der Waals wells, so the magnitude of the difference potential $|V_{20}|$ was much smaller, and the adiabatic limit remained dominant down to smaller $|s|$ values. Population transfer could still occur for small $|s|$, but the coupling arises from the difference potential in the more repulsive region near the barrier, and the transition between adiabatic and statistical limits occurs much more rapidly.

**C. Transition State Resonances**

We now consider the resonance structures in Figs. 2 and 3. We begin by recalling from the Introduction that past (single surface) studies of ClHCl using the BCMR surface[20] have observed one significant resonance feature over the energy range considered[8], namely a peak near E=0.642 eV with a full width at half maximum of about 0.004 eV. This resonance has been assigned the saddle point quantum numbers $(\nu_1,\nu_2,\nu_3) = (0,0,2)$. A similar resonance is seen in exact quantum calculations for linear ClHCl, as well as resonances at higher energies that correspond to higher excitations of the $\nu_3$ mode; the lower energy resonances, e.g., for $\nu_3$=0, are not sufficiently stable to show narrow structure.[20] Note also that there are no progressions in either symmetric stretch or bend quantum numbers associated with the (0,0,2) resonance on the BCMR surface.[7]

The results in Fig. 2(d) for s=1.0 are similar to what we have just described for the BCMR surface, except that the resonance occurs at E=0.58 eV rather than at 0.642 eV, and there is an excited state at 0.61 eV. To understand these results, we have performed additional 244 state calculations (not shown) in which the interaction potential $V_{21}$ is set to zero everywhere, but no other parameters are changed. We find that the resulting cumulative probabilities are very similar to those in Fig. 2(d). This suggests that the E=0.58 eV resonance is not associated with the coupled multisurface nature of the dynamics, and is therefore the analogue of the (0,0,2) resonance seen in BCMR calculations. It occurs at a lower energy than for BCMR, in spite of the somewhat higher barrier height (0.393 eV for the $\Sigma$ diabat versus 0.371 eV for BCMR), because the resonance is probably delocalized over a broader region of space which includes the van der Waals wells. Further support for this idea can be gained by noticing that only the $j=j'=3/2$ cumulative probability is strongly perturbed by this resonance for s=1.0. For s=-0.5, it is the $j=j'=1/2$ cumulative probability that is strongly perturbed, which is consistent with the adiabatic correlations that occur when the $^2P_{1/2}$ state is of lowest energy, as discussed near the end of Section IV.B.

If this assignment of the resonance is correct, then the higher energy resonance can be assigned as a bend excited state of the $\Sigma$ diabat transition state, based on the behavior of cumulative probabilities where the value of the initial and final values of $\Omega_N$ are specified. These cumulative probabilities show that for s = 1.0 the resonance at E=0.58 eV is associated with $\Omega_N = \Omega_{N'} = 0$, as one would expect for the ground bend state, while that at E=0.61 eV is exclusively $\Omega_N = \Omega_{N'} = 1$, which corresponds to the one quantum of vibrational angular momentum for the first excited bend state. Note that $\Omega_N=1$ states are included in the J=1/2 basis set, along with $\Omega_N=0$ and $\Omega_N=2$, so the excited bend states with $\Omega_N=1$ are allowed in our calculation, whereas they would not be present in single surface calculations where J=0. The energy shift between the ground and first excited bend states is thus $\approx$0.03 eV, which is substantially smaller than the energy shift using the harmonic saddle point bending energy of 0.09 eV on the $\Sigma$ diabat, but it is likely that the resonance is considerably delocalized away from the saddle point region to geometries in the van der Waals wells where the effective bend energy will be much smaller. For s=-0.5, a similar analysis of the dependence of the cumulative probabilities on $\Omega_N$ gives similar results, namely that the lowest energy resonance mostly perturbs the $\Omega_N$=0 probabilities and the next one perturbs $\Omega_N$=1. However the separation between the two $\Omega_N$'s is not as clean as for s=1.0. This suggests stronger nonadiabaticity for negative s, which is consistent with comparisons of Figs 4(a) and 4(d) presented in Sect. IV.B

Another clue comes in comparing the graphs in Fig. 3 (a)-(d). The position of the lowest resonance energy varies with s as if determined by the properties of the $\Sigma$ diabatic barrier relative to $^2P_{3/2}$, namely $E^J_{res}(s) = E^J_{res}(0)-\frac{1}{2}s\lambda_{Cl}= E^J_{res}(0)+(0.0363eV)s$. This relation says that the s=1.0 resonance energy should be 0.055 eV higher than the s=-0.5 one, which is what we find. Notice also in Fig. 3 that the resonances are quite distinct for s=-0.5 and 1.0, but are barely discernable (i.e., broader) for s = 0.0 and 0.1. This broadening of the resonances for small $|s|$ is most likely due to the strong coupling between different fine structure components that occurs in this limit. This coupling mixes together the states that support the resonance (those correlating with the $\Sigma_{1/2}$ near the transition state) with those that produce resonance decay ($\Pi_{1/2}$), which is presumably what produces the broader resonances.

**D. Rate coefficients**

Figure 6 presents an Arrhenius plot for the thermal rate coefficient k(T) which is derived from $P^J_{cum}(E)$ for J = ½ using Eqs. (17)-(19). Also shown are normalized rate coefficients (defined below) for the three (j, j′) combinations considered in Figs. 2-4. The rate coefficients are calculated from the 244 state cumulative probabilities shown in Fig. 3, and are for the scale factors s = -0.5, 0.0, 0.1 and 1.0. Over the temperature range 300-1200 K, the s=1.0 rate coefficients agree with those from the 292 state calculations to within 20%, so we have not plotted the 292 state results separately. In Ref. 6 we compared very similar 244 state rate coefficients for s=1.0 with results from earlier single surface calculations, with quasiclassical trajectory calculations and with experimental data, so we omit a discussion here.

The normalized state-selected rate coefficients are defined by

$$k^{norm}(T;j,j') = \frac{Q^{e\ell}_{reag}(T;j)}{Q^{e\ell}_{reag}(T)} k(T;j,j') \tag{21}$$

where from Sect. III.E,

$$k(T;j,j') = \frac{1}{hQ^{nu}_{reag}(T)Q^{e\ell}_{reag}(T;j)} \int_0^\infty P_{cum}(E;j,j') \exp(-E/k_B T)\, dE \tag{22}$$

It follows from the definition (21) that

$$k(T) = \sum_{jj'} k^{norm}(T;j,j') \tag{23}$$

Relation (23) has the advantage that it simplifies Arrhenius plots, since it is easier to see how different spin states contribute to the total rate coefficient k(T). Furthermore, the normalized rate coefficients for $j = 3/2 \rightarrow j' = 1/2$ and $j = 1/2 \rightarrow j' = 3/2$ are equal, so we only need plot one of them.

The k(T)'s in Fig. 6 show typical Arrhenius behaviour, with a dependence on s which, for positive s, is easily described using the simple energy shift of the $^2P_{3/2}$ state by the spin-orbit interaction, i.e.,

$$k(T,s>0) = k(T,s=0)\exp(-\frac{1}{2}s|\lambda_{Cl}|/k_B T) \tag{24}$$

For negative s, we need to take into account the fact that $^2P_{1/2}$ is the lowest energy state, and the barrier relative to this state increases as s increases. In this case the energy shift is twice what it is when $^2P_{3/2}$ is the ground state, so Eq. (24) is replaced by

$$k(T,s<0) = k(T,s=0)\exp(s|\lambda_{Cl}|/k_B T) \tag{25}$$

The normalized rate coefficients in Fig. 6 show considerable variation with s, as expected from our analysis of Figs. 3 and 4, with the 3/2→3/2 result being dominant for s = 1.0. All three rate coefficients are comparable in magnitude for s = 0.1. The s = 0.0 result shows the expected 4:2:1 ratio (see Sect. IV.B), and 1/2→1/2 is dominant for s =-0.5 (for T<600K). For s=1.0, at 300 K, the normalized 1/2→1/2 rate coefficient is only 0.7% of k(T), 3/2→1/2 is 3.5% of k(T), and 3/2→3/2 is 92.3% of k(T). The corresponding percentages for s = 0.1 are 34.1%, 22.4% and 21.0% while for s=-0.5 they are 41.6%, 17.8% and 22.9%.

## V. Conclusions

This paper has explored two interrelated aspects of the $Cl(^2P_j)$ + HCl reaction, and more generally of open shell atoms colliding with closed shell diatomic molecules. Firstly, we have studied the evolution of the asymptotic fine structure states towards the barrier region, and the way in which this influences the fine-structure resolved reactivity. Our results in Fig. 5 indicate that there are many different kinds of behaviour which are primarily determined by the magnitude of the van der Waals well depth (which determines the "difference potential" $V_{20}$ which couples the states at large distances) compared to the magnitude of the spin-orbit coupling constant (which determines the splitting of the asymptotic states). When the spin-orbit constant is negative, and the splitting is larger than the van der Waals well depth, as happens for "real" chlorine atom reactions, the dynamics is predominantly adiabatic, which means that the reactivity of the $^2P_{1/2}$ state is much smaller (few percent) than $^2P_{3/2}$. Adiabatic dynamics is also recovered for large positive values of the spin-orbit constant, but in this limit it is the $^2P_{1/2}$ state that has the larger reactivity, at least close to the reaction threshold. (See Fig. 4.) If the spin-orbit constant is zero (or much smaller than the van der Waals well depth), then the fine structure states are strongly mixed, and the fine structure propensities are controlled by simple statistics. This means that $^2P_{3/2}$, with its greater degeneracy, has higher reactivity. There is an intermediate regime between the statistical and adiabatic limits, where nonadiabatic coupling produces "inverted" propensities, where for negative spin-orbit parameters the $^2P_{1/2}$ state has the higher reactivity, whilst for positive parameters the $^2P_{3/2}$ state has the higher reactivity. This behaviour is found for both cumulative probabilities and thermal rate coefficients.

The second aspect of the $Cl(^2P_j)$ + HCl reaction that we studied are transition state resonances. We found that using coupled potential surfaces does not change the resonance spectrum much compared to the single surface result. In particular, we find that the two lowest energy resonances correspond to the asymmetric stretch excited state (0,0,2), and the state (0,1,2) having one quantum of bend excitation.

The connection between the present results and experiment is an important task for future studies. The small $^2P_{1/2}$ reactivity that we find when the true chlorine spin-orbit parameter is used has often been observed in chlorine atom reactions;[13] it will be interesting to study reactions that exhibit the more dramatic effects that we have predicted. Our results indicate that these effects should occur in atoms whose spin-orbit parameters have smaller magnitudes, such as are found in the first row of the periodic table.

The experimental observation of transition state resonances of any type has proven to be a major experimental challenge. However, ClHCl is a candidate for such observation through photodetachment spectroscopy.[9] Recently an improved formalism for calculating photodetachment spectra in $ClHCl^-$ has been presented[22], so an important task for future theoretical work will be the implementation of this theory (e.g., using the wavefunctions generated with the scattering code described in this paper). Before this is done, however, it will be necessary to check the accuracy of the potential energy surfaces and couplings that we have used. This should be possible soon, as Besley and Knowles[23] have recently performed *ab initio* calculations for this reaction that provide both surfaces and couplings of higher quality than have been available previously.

## VI. Acknowledgements

This research was supported by the U. S. Department of Energy, Office of Basic Energy Sciences, Division of Chemical Sciences, under Contract No. W-31-109-ENG-38, and by the UK Science and Engineering Research Council. We thank Dr. A. J. Dobbyn for many important comments.

## References


1. H. Nakamura, *Int. Rev. Phys. Chem.* 1991, **10**, 123; M. Baer, *Theory of Chemical Reaction Dynamics*, Vol. II, ed. M. Baer, CRC Press, Boca Raton, FL, 1985, Chap. 4.

2. M. Gilibert and M. Baer, *J. Phys. Chem.* 1994, **98**, 12822; *ibid.* 1995, **99**, 15748; D. M. Charutz, R. Baer and M. Baer, *Chem. Phys. Lett.* 1997, **265**, 629; R. Baer, D. M. Charutz, R. Kosloff and M. Baer, *J. Chem. Phys.* 1996, **105**, 9141; I. Last, M. Gilibert and M. Baer, *J. Chem. Phys.* 1997, **107**, 1451.

3. G. C. Schatz, *J. Phys. Chem.* 1995, **99**, 7522. In Eq. (2) for $+2\mathbf{N}\cdot\mathbf{j}$ read $-2\mathbf{N}\cdot\mathbf{j}$. In Table 1, for $v_{00}$, $v_{20}$ read $V_{00}$, $V_{20}$. In Section IV, for $\lambda$ read $|\lambda|$. In the caption to Fig. 3, for ref. 24, read ref. 25. In Ref. 25, for **91**,5496, read **93**, 251.

4. S. L. Mielke, G. J. Tawa, D. G. Truhlar and D. W. Schwenke, *Chem. Phys. Lett.* 1995, **234**, 57; S. L. Mielke, D. G. Truhlar and D. W. Schwenke, *J. Phys. Chem.* 1995, **99**, 16210; M. S. Topaler, M. D. Hack. T. C. Allison, Y. -P. Liu, S. L. Mielke, D. W. Schwenke and D. G. Truhlar, *J. Chem. Phys.* 1997, **106**, 8699; T. C. Allison, S. L. Mielke, D. W. Schwenke and D. G. Truhlar, *J. Chem. Soc. Faraday Trans.* 1997, **93**, 825.

5. J. Qi and J. M. Bowman, *J. Chem. Phys.* 1996, **104**, 7545; A. J. C. Varandas and H. G. Yu, *Chem. Phys. Lett.* 1996, **259**, 336; T. J. Martínez, *Chem. Phys. Lett.* 1997, **272**, 139.

6. C. S. Maierle, G. C. Schatz, M. S. Gordon, P. McCabe and J. N. L. Connor, *J. Chem. Soc. Farad. Trans.* 1997, **93**, 709. On p. 712, for $\gamma$=152° read $\theta$=152°; in Eq. (2) for $+2\mathbf{N}\cdot\mathbf{j}$ read $-2\mathbf{N}\cdot\mathbf{j}$; below eqn. (11), for substitution of eqn. (1) read substitution of eqn. (10); in Fig. 6, for $P^J_{cum}(E;_1 1/2,1/2)$ read $P^J_{cum}(E; 1/2,1/2)$; in Figs. 4(c) and 4(d), for ClCHI read ClHCl.

7. G. C. Schatz, D. Sokolovski and J. N. L. Connor, in *Advances in Molecular Vibrations and Collision Dynamics*, Vol 2B, Ed. J. M. Bowman, JAI Press, Greenwich, CT, 1994, pp. 1-26.

8. J. N. L. Connor, P. McCabe, D. Sokolovski and G. C. Schatz, *Chem. Phys. Lett.* 1993, **206**, 119; G. C. Schatz, D. Sokolovski and J. N. L. Connor, *Can. J. Chem.* 1994, **72**, 903; D. Sokolovski, J. N. L. Connor and G. C. Schatz, *Chem. Phys. Lett.* 1995, **238**, 127; *J. Chem. Phys.* 1995, **103**, 5979; *Chem. Phys.* 1996, **207**, 461; N. Rougeau and C. Kubach, *Chem. Phys. Lett.* 1994, **228**, 207; A. B. McCoy, *Mol. Phys.* 1995, **85**, 965; M. J. Cohen, A. Willetts and N. C. Handy, *J. Chem. Phys.* 1993, **99**, 5885; A. Laganà, A. Aguilar, X. Gimenez and J. M. Lucas, in *Advances in Molecular Vibrations and Collision Dynamics*, Vol. 2A, Ed. J. M. Bowman, JAI Press, Greenwich, CT, 1994, pp. 183-201.

9. R. B. Metz, T. Kitsopoulos, A. Weaver and D. M. Neumark, *J. Chem. Phys.* 1988, **88**, 1463; R. B. Metz, A. Weaver, S. E.Bradforth, T. N. Kitsopoulos and D. M. Neumark, *J. Phys. Chem.* 1990, **94**, 1377.

10. F. Rebentrost and W.A. Lester Jr. *J. Chem. Phys.* 1975, **63**, 3737; 1976, **64**, 3879; 1976, **64**, 4223; 1977, **67**, 3367; F. Rebentrost, in *Theoretical Chemistry: Advances and Perspectives*, ed. D. Henderson, Vol. 6B, Theory of Scattering: Papers in Honor of Henry Eyring, Academic, New York, 1981, pp. 1-77.

11. M. -L. Dubernet and J. M. Hutson, *J. Phys. Chem.* 1994, **98**, 5844.

12. L. Visscher and K. G. Dyall, *Chem. Phys. Lett.* 1995, **239**, 181.

13. D. Husain and R. J. Donovan, *Adv. Photochem.* 1971, **8**, 1; R. J. Donovan and D. Husain, *Chem. Rev.* 1970, **70**, 489; P. J. Dagdigian and M. L. Campbell, *Chem. Rev.* 1987, **87**, 1; P. J. Dagdigian in *Selectivity in Chemical Reactions*, Proceedings of the NATO Advanced

Research Workshop, Bowness-on-Windermere, UK, 7-11 September 1987, Ed. J. C. Whitehead, Kluwer, Dordrecht, 1988, pp. 147-177; A. González-Ureña and R. Vetter, *J. Chem. Soc. Faraday Trans.* 1995, **91**, 389; M. Alagia, N. Balucani, P. Casavecchia, D. Stranges and G. G. Volpi, *J. Chem. Soc. Faraday Trans.* 1995, **91**, 575.

14. G. C. Schatz, *J. Phys. Chem.* 1990, **94**, 6157.

15. G. C. Schatz and A. Kuppermann, *J. Chem. Phys.* 1976, **65**, 4642; G. C. Schatz, L. M. Hubbard, P. S. Dardi and W. H. Miller, *J. Chem. Phys.* 1984, **81**, 231.

16. L. M. Delves, *Nucl. Phys.* 1959, **9**, 391; 1960, **20**, 275.

17. G. C. Schatz, *Chem. Phys. Lett.* 1988, **150**, 92.

18. H. Koizumi and G. C. Schatz, in *Advances in Molecular Vibrations and Collision Dynamics,* Vol. 1A, Ed. J. M. Bowman and M. A. Ratner, JAI Press, Greenwich, CT, 1991, pp. 139.-164.

19. Q. Sun, J. M. Bowman, G. C. Schatz, J. R. Sharp, and J. N. L. Connor, *J. Chem. Phys.* 1990, **92**, 1677; M. C. Colton and G. C. Schatz, *Int. J. Chem. Kinet.* 1986, **18**, 961.

20. D. K. Bondi, J. N. L. Connor, J. Manz and J. Römelt, *Mol. Phys.* 1983, **50**, 467.

21. G. C. Schatz, *J. Chem. Phys.*1989, **90**, 3582.

22. G. G. Balint-Kurti and G. C. Schatz, *J. Chem. Soc. Faraday Trans.* 1997, **93**, 755.

23. N. A. Besley and P. J. Knowles, 1998, private communication.

**Table 1.** Electronic Matrix Elements. Only the upper portion is shown because the matrix is symmetric.

| $j'\ \Omega_{j'}$ \ $j\ \Omega_j$ | 3/2 3/2 | 3/2 1/2 | 3/2 -1/2 | 3/2 -3/2 | 1/2 1/2 | 1/2 -1/2 |
|---|---|---|---|---|---|---|
| 3/2 3/2 | $V_{00}-\frac{1}{5}V_{20}$ | $-\frac{\sqrt{2}}{5}V_{21}$ | $-\frac{\sqrt{2}}{5}V_{22}$ | 0 | $\frac{1}{5}V_{21}$ | $\frac{2}{5}V_{22}$ |
| 3/2 1/2 | | $V_{00}+\frac{1}{5}V_{20}$ | 0 | $-\frac{\sqrt{2}}{5}V_{22}$ | $\frac{-\sqrt{2}}{5}V_{20}$ | $-\frac{\sqrt{3}}{5}V_{21}$ |
| 3/2 -1/2 | | | $V_{00}+\frac{1}{5}V_{20}$ | $\frac{\sqrt{2}}{5}V_{21}$ | $-\frac{\sqrt{3}}{5}V_{21}$ | $\frac{\sqrt{2}}{5}V_{20}$ |
| 3/2 -3/2 | | | | $V_{00}-\frac{1}{5}V_{20}$ | $-\frac{2}{5}V_{22}$ | $\frac{1}{5}V_{21}$ |
| 1/2 1/2 | | | | | $V_{00}-\frac{3}{2}\lambda$ | 0 |
| 1/2 -1/2 | | | | | | $V_{00}-\frac{3}{2}\lambda$ |

## Figure Captions

Figure 1. Schematic profiles of the potential surfaces for linear ClHCl along the reaction path joining reagents and products. (a) non-relativistic profiles (b) relativistic profiles which include the spin-orbit interaction.

Figure 2. Cumulative reaction probability $P^J_{cum}(E)$ (thick solid curve) for J = ½ and state-selected cumulative reaction probabilities $P^J_{cum}(E;j,j')$ for J = ½ versus total energy E with (j,j')=(1/2,1/2) (dashed),(3/2,1/2) (dotted), (3/2,3/2) (solid) and a linear scaling factor of s=1.0 (a) results for 244 states, (b) results for 292 states.

Figure 3. Same as Fig. 2 for 244 states except that (a) s=-0.5, (b) s= 0.0, (c) s= 0.1, (d) s=1.0.

Figure 4. $P^J_{cum}(E)$ and $P^J_{cum}(E;j,j')$ for 172 states with J = ½ , E = 0.40 eV, versus the linear scaling parameter s.

Figure 5.(a) Adiabaticity parameter $\zeta$ versus Jacobi coordinate R for $r_{HCl} = 2.40\ a_0$ and linear ClHCl, (b) adiabats associated with the electronic Hamiltonian for $\Omega_j$=1/2 ($^2\Sigma_{1/2}$ (solid curve) and $^2\Pi_{1/2}$ (dotted)), and for $\Omega_j$=3/2 ($^2\Pi_{3/2}$ (dashed)) as a function of the Jacobi coordinate R, for r=2.40 $a_0$ and linear ClHCl. The adiabats have been labelled in the same way as Fig. 1.

Figure 6. Arrhenius plot of the thermal rate coefficient log k(T) versus 1/T (thick solid line). Also plotted are the normalized fine-structure rate coefficients log $k^{norm}(T;j,j')$, for j = 3/2 → j' = 3/2 (solid), j = 3/2 → j' = 1/2 (dotted), and j = 1/2 → j' = 1/2 (dashed). Note that $k^{norm}(T;j=3/2, j'=1/2) \equiv k^{norm}(T;j=1/2, j'=3/2)$. All results are from calculations using 244 states.

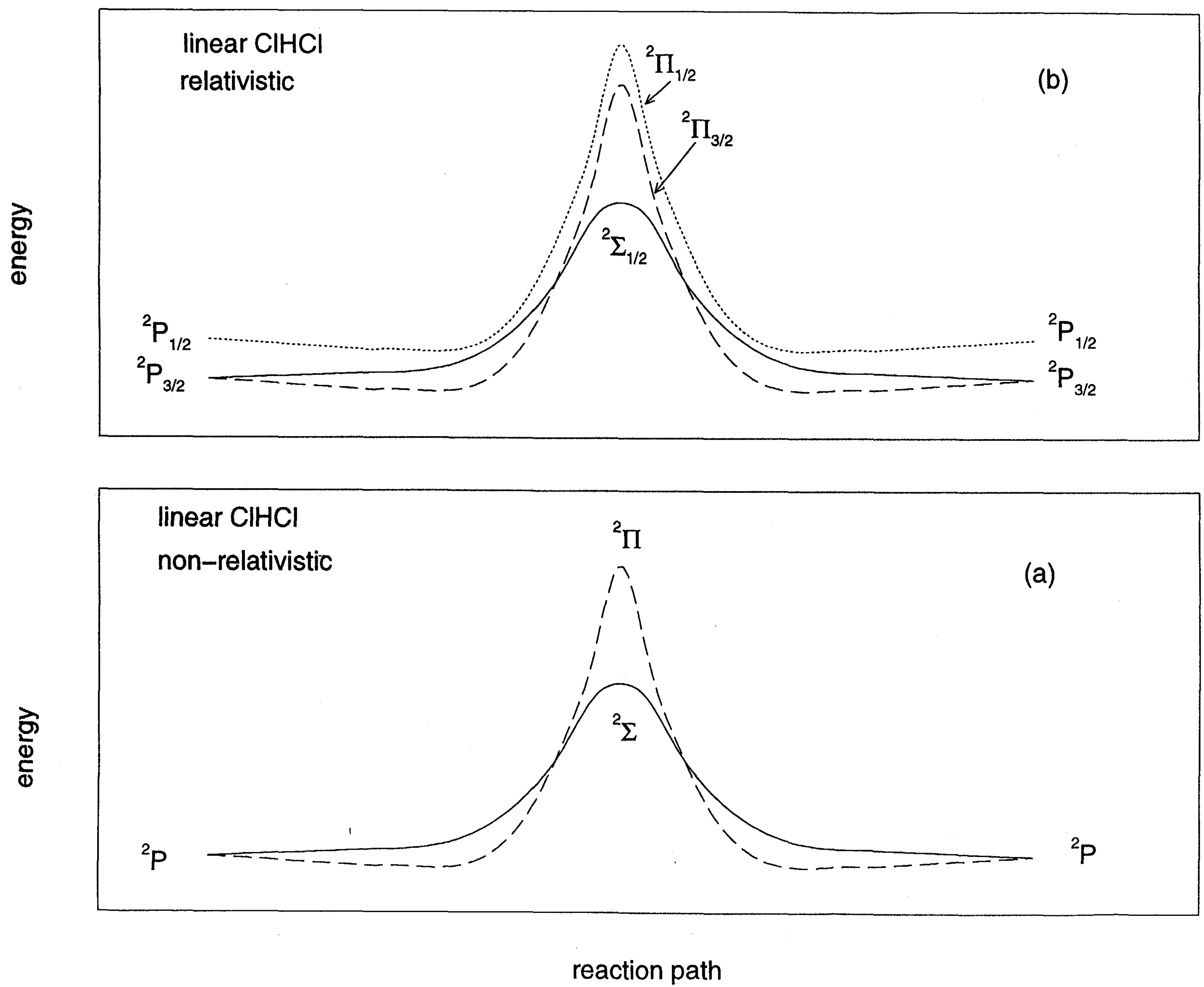

linear ClHCl
relativistic
(b)
$^2\Pi_{1/2}$
$^2\Pi_{3/2}$
$^2\Sigma_{1/2}$
$^2P_{1/2}$
$^2P_{3/2}$
$^2P_{1/2}$
$^2P_{3/2}$
energy
linear ClHCl
non–relativistic
(a)
$^2\Pi$
$^2\Sigma$
$^2P$
$^2P$
energy
reaction path

Fig. 1

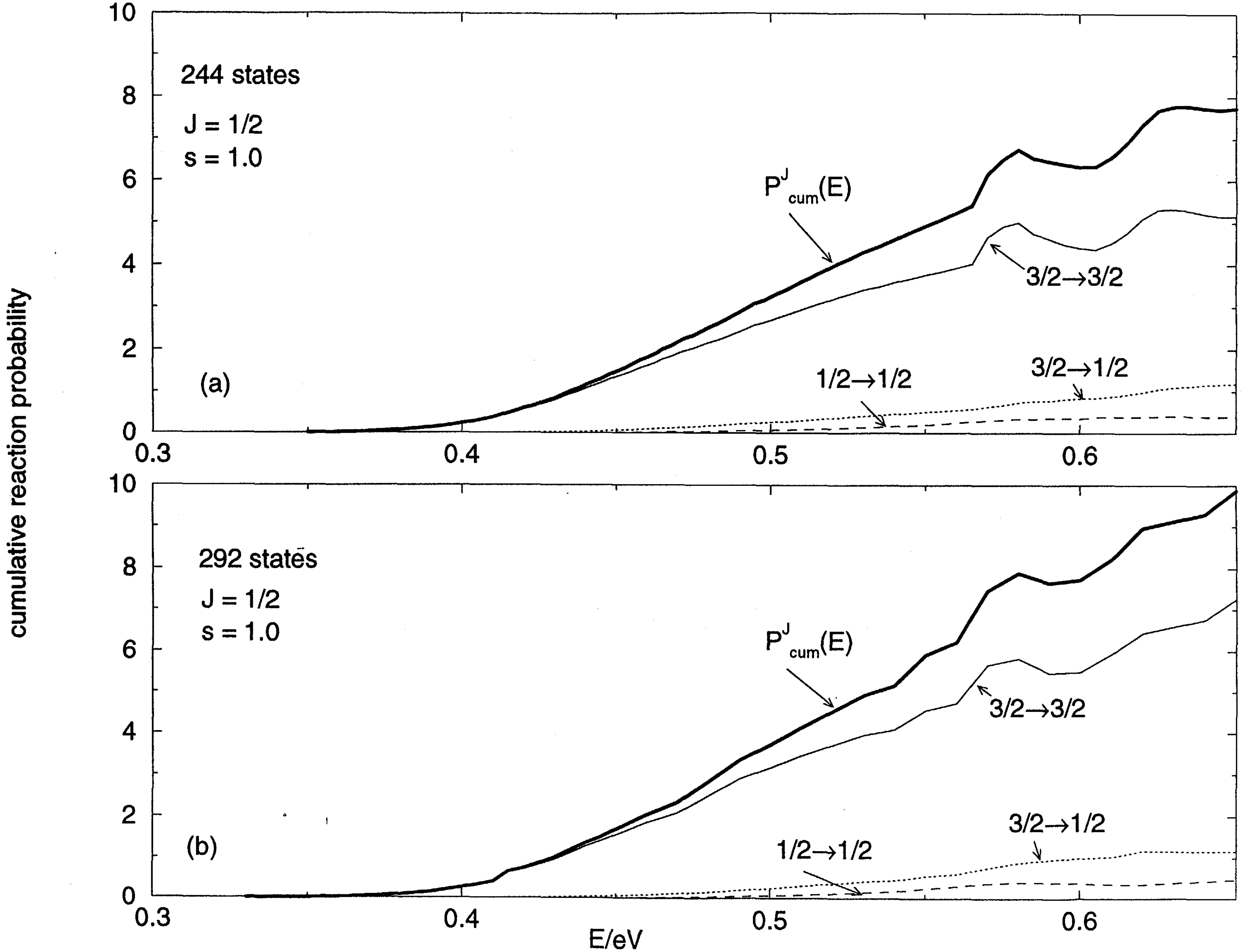

cumulative reaction probability
244 states
J = 1/2
s = 1.0
(a)
$P^J_{cum}(E)$
3/2→3/2
1/2→1/2
3/2→1/2
292 states
J = 1/2
s = 1.0
(b)
$P^J_{cum}(E)$
3/2→3/2
1/2→1/2
3/2→1/2
E/eV


Fig. 2

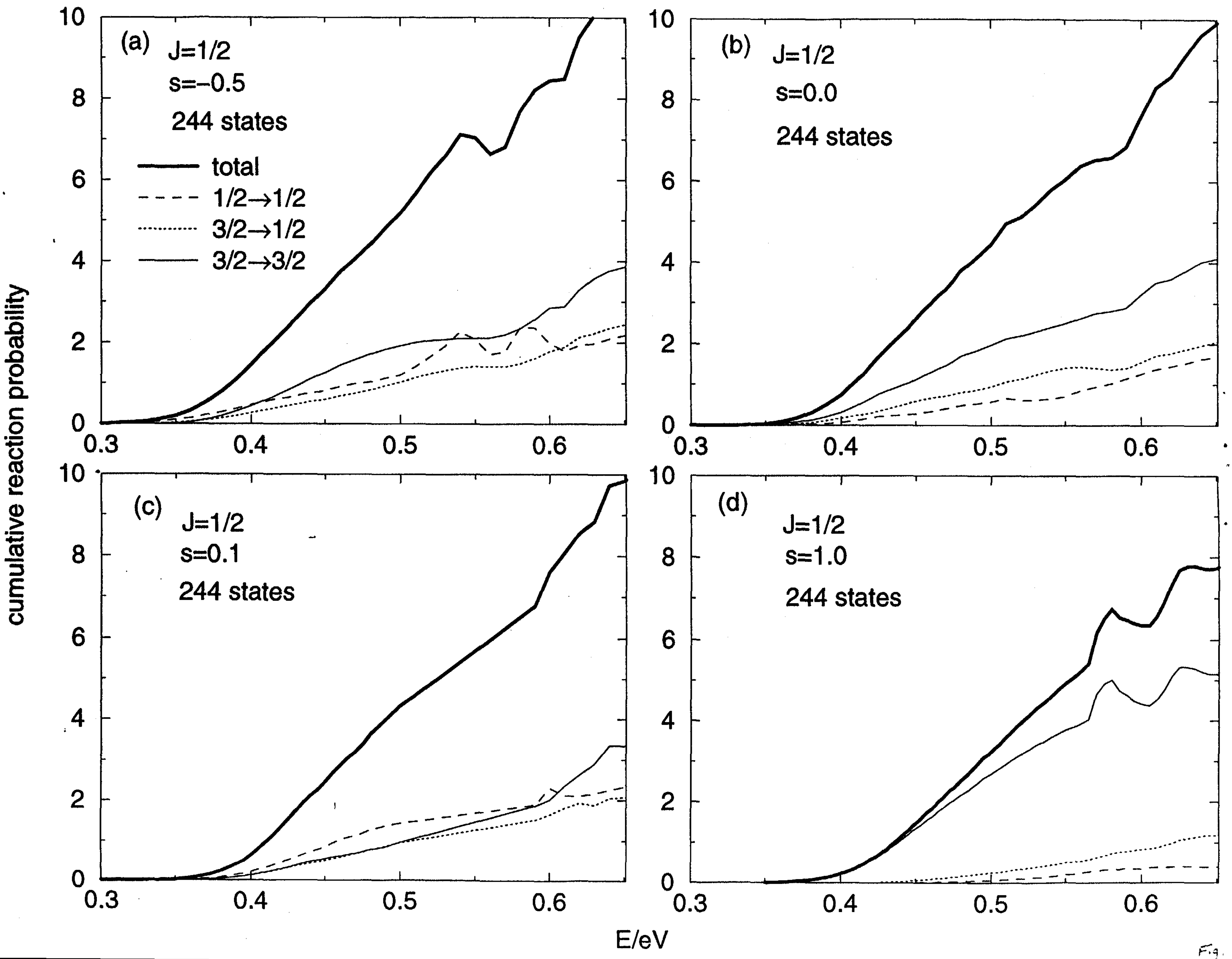

(a) J=1/2
s=−0.5
244 states
total
1/2→1/2
3/2→1/2
3/2→3/2
(b) J=1/2
s=0.0
244 states
(c) J=1/2
s=0.1
244 states
(d) J=1/2
s=1.0
244 states
cumulative reaction probability
E/eV


Fig. 2

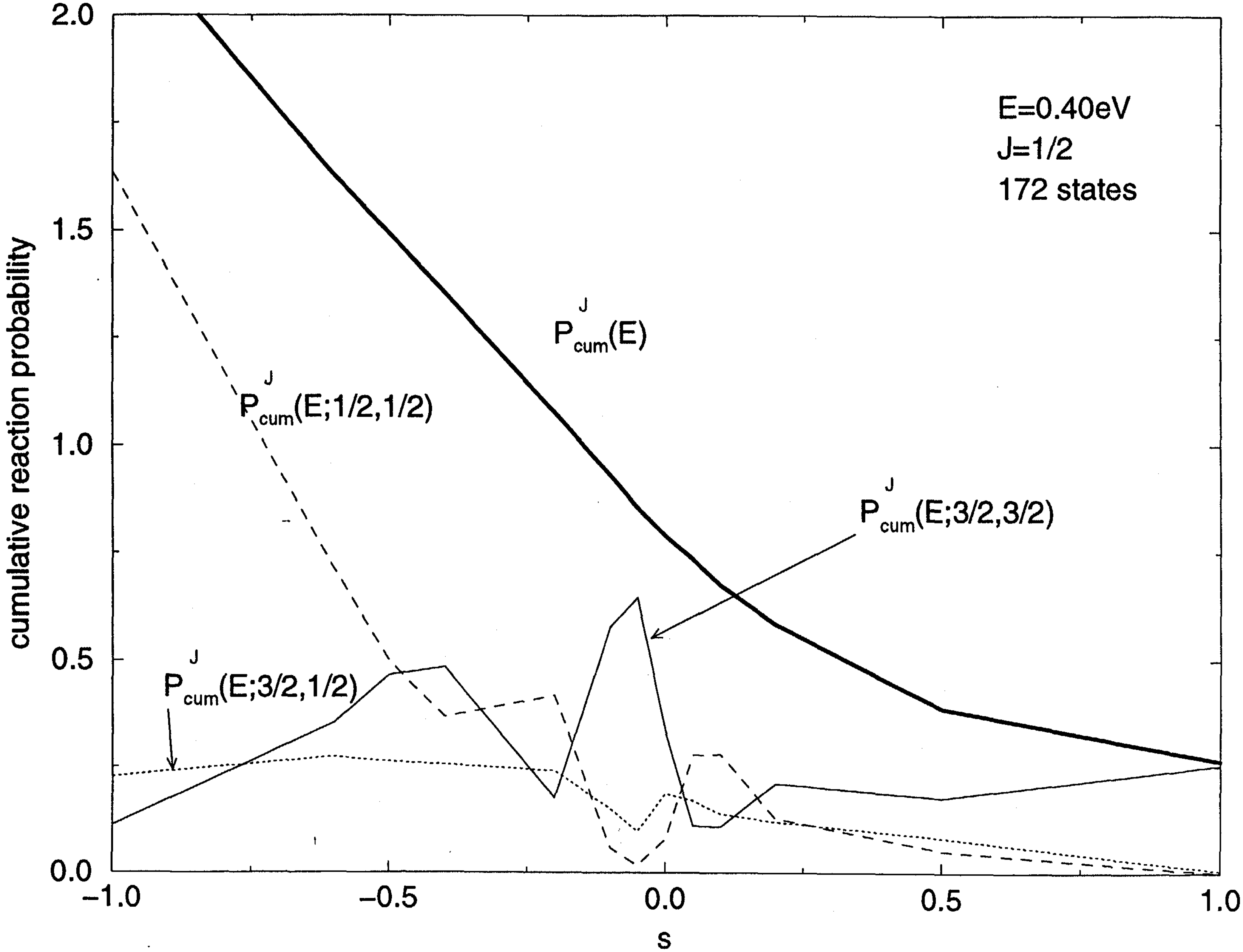

E=0.40eV
J=1/2
172 states
$P^J_{cum}(E)$
$P^J_{cum}(E;1/2,1/2)$
$P^J_{cum}(E;3/2,3/2)$
$P^J_{cum}(E;3/2,1/2)$
cumulative reaction probability
s


Fig 4

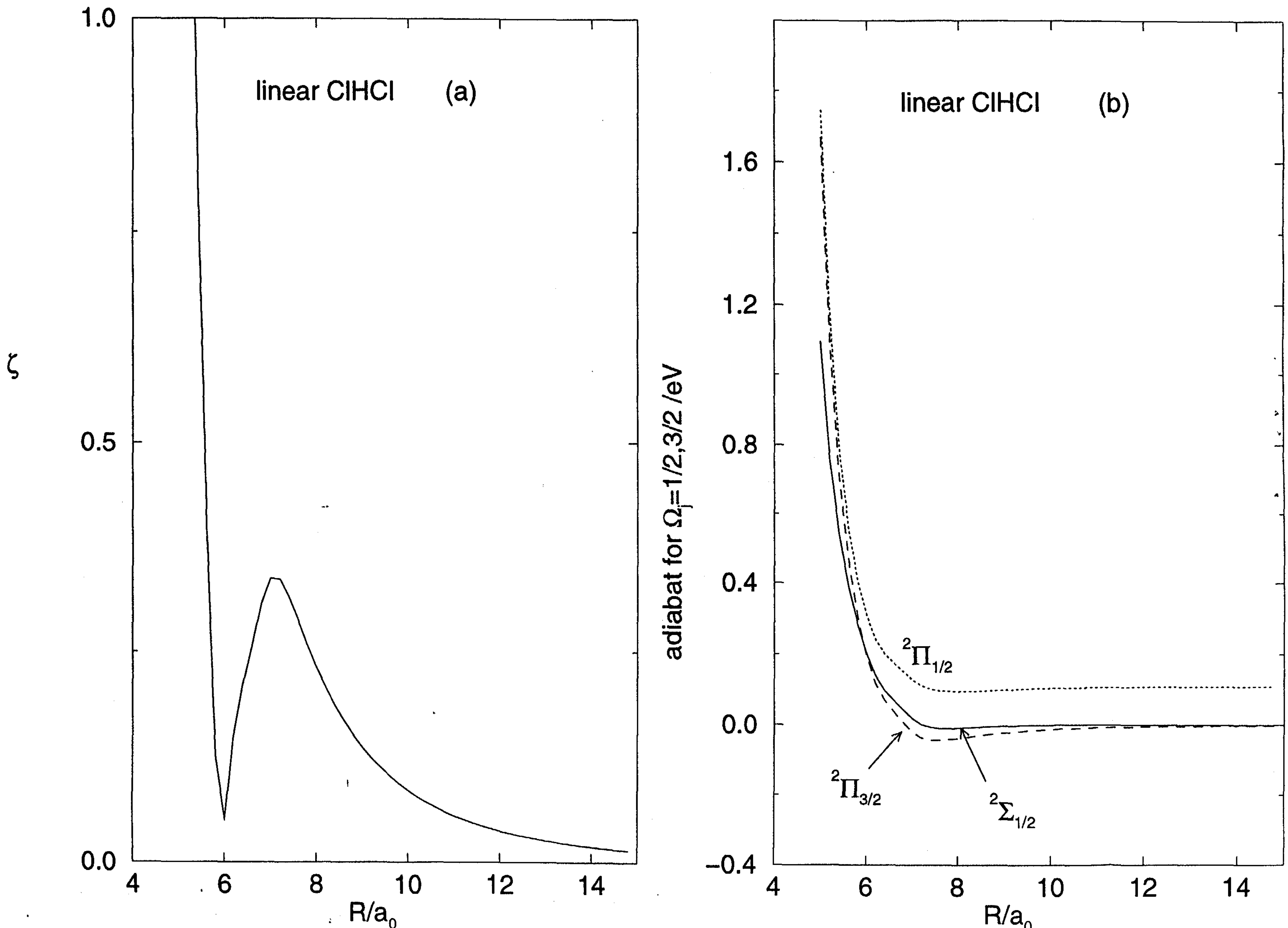
linear ClHCl (a)
ζ
1.0
0.5
0.0
4
6
8
10
12
14
R/a0
linear ClHCl (b)
adiabat for Ωj=1/2,3/2 /eV
1.6
1.2
0.8
0.4
0.0
−0.4
2Π1/2
2Π3/2
2Σ1/2

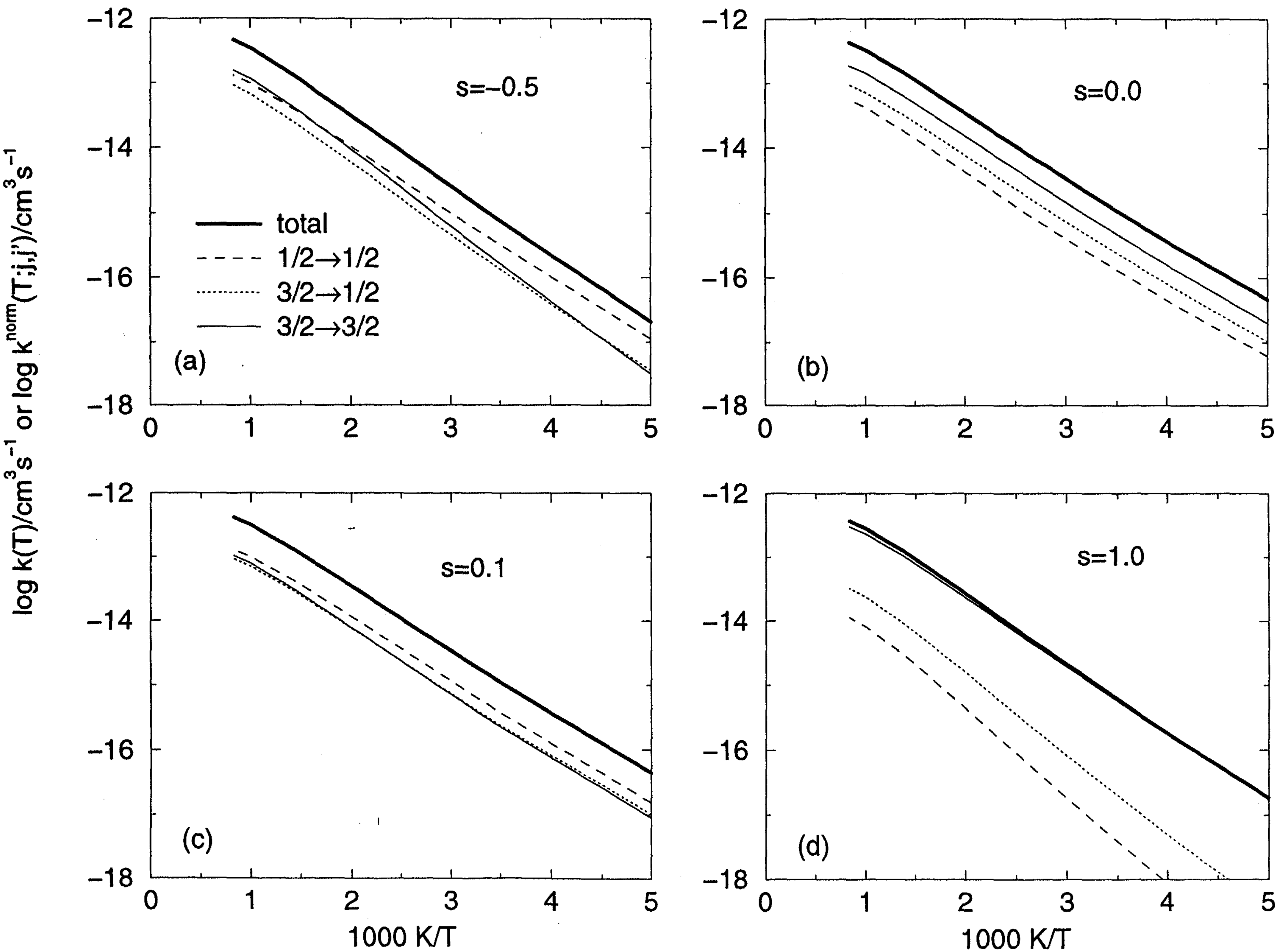
log k(T)/cm$^3$s$^{-1}$ or log k$^{norm}$(T;j,j')/cm$^3$s$^{-1}$
total
1/2→1/2
3/2→1/2
3/2→3/2
s=−0.5
s=0.0
s=0.1
s=1.0
(a)
(b)
(c)
(d)
1000 K/T
1000 K/T